Journal of Magnetism and Magnetic Materials xx (2022) xx

Contents lists available at ScienceDirect

Journal of Magnetism and Magnetic Materials

journal homepage: www.elsevier.com/locate/addlet

Evaluation of 3D-Printed Magnetic Materials For Additively-Manufactured Electrical Machines

Ahmed Selema [a,b,*], Margherita Beretta [a,c], Matty Van Coppenolle [a,b], Hans Tiismus [e], Ants Kallaste [e], Mohamed N. Ibrahim [a,b], Marleen Rombouts [d], Jozef Vleugels [c], Leo A.I. Kestens [a,b], Peter Sergeant [a,b]

[a] *Department of Electromechanical, Systems, and Metal Engineering, Ghent University, 9000 Ghent, Belgium*
[b] *FlandersMake@UGent, Core Lab EEDT-MP, 3001 Leuven, Belgium*
[c] *Department of Materials Engineering, KU Leuven, Kasteelpark Arenberg 44, 3001 Heverlee, Belgium*
[d] *Flemish Institute for Technological Research - VITO, Boeretang 200, 2400 , Mol, Belgium*
[e] *Department of Electrical Power Engineering and Mechatronics, Tallinn University of Technology, Ehitajate tee 5, 19086 Tallinn, Estonia*

ARTICLE INFO

Keywords:
Additive manufacturing
Electrical machines
3D printed Fe-Si
Magnetic material

ABSTRACT

Nowadays, going beyond the 2D conventionally laminated structures is essential for improving the functionality of an electrical machine during the design process. Additive manufacturing (AM) offers unmatched 3D freedom for processing metal-based materials optimized for weight and cost effectiveness. Using this technology, new families of electrical machines can be manufactured which are difficult to be built using conventional methods. This paper is mainly targeting printing and testing of ferromagnetic material. Using different AM techniques, different parts are built using the silicon steel (Fe-3wt%Si) powder. The magnetic properties of these parts are measured and compared. Accordingly, a proper AM technology is identified as a promising method to manufacture magnetic materials. Additionally, quasi-static measurements are performed at low frequencies to compare the hysteresis losses of the 3D printed samples with those in conventional Fe-Si laminations. Results shows that good magnetic properties can be obtained from the 3D printed samples. Finally, the potential of 3D multi-material printing is highlighted for electrical machines.

1. Introduction

1.1. Electrical Machines Manufacturability: Present and Future

Over the years, electrical machines have been improving rapidly targeting compactness, high efficiency, and high power density [1]. Yet, modern machines are still counting on traditional manufacturing techniques that go back to the 1830s. With the limited capabilities of these methods, the manufacturability of electrical machines is negatively impacted.

Electrical machines are traditionally made from thin steel laminations which are stacked in an extruded 2D layout process. Using these conventional production methods, the electrical steel sheets have been extensively investigated and optimized for improved magnetic properties along with weight and cost effectiveness. In such process, XY plane is fully used in terms of dimensions and magnetic material orientation, but the third dimension is not. Moreover, material and mass optimization are limited. Therefore, new production techniques have to be considered to explore the third dimension along with materials engineering to design efficient electrical machine components. Using additive manufacturing (AM), topology-optimized machines can be designed into a true 3D form with improved electromagnetic isotropy in X,Y and Z.

Metal-based AM has been explored in different studies for electrical machines [2,3]. Moreover, the manufacturing of new families of electrical machines which were difficult to be built using conventional methods was attempted [4–6]. Yet, utilizing AM in building the active parts such as core or windings is still limited. Those parts have to fulfill different needs both in terms of electromagnetic and mechanical properties.

1.2. A Case Study: YASA Axial Flux Machine

Among different non-conventional electrical machines, the Yokeless and Segmented Armature (YASA) Axial flux machine is an attractive choice due to its high power density [7–9]. The complete machine configuration is shown in Fig. 1. One of the main challenges of the YASA machines is that the stator segments are made of radially-stacked laminations. So, the width of each single lamination should be decreasing from the outer to the inner radius. In other words, each lamination must have a different shape in order to carry the axially-directed flux. Typically, this is addressed by using different laminations widths [10,11]. However, it is rather difficult to get a neat final shape. Besides, the uneven lamination assembly is extremely time consuming during the production process especially without automated assembly [12]. So, when a core module of a YASA machine is prototyped, manufacturers try to limit the number of different lamination shapes in order to save time and effort during the assembly processes. With the emergence of new technologies such as Additive Manufacturing (AM), such challenges can be addressed more successfully and new design possibilities are enabled with easier manufacturability and more degrees of freedom.

* Corresponding author.
E-mail addresses: ahmed.selema@ugent.be , selema@ieee.org.

https://doi.org/10.1016/xxxxxxxxxxxxxx
Received xx July 2022; Received in revised form xx 2022
2772-3690/

Using 3D Finite element modeling, the aforementioned design is simulated as shown in Fig. 2. Interestingly, it is found that the axially-directed flux is not parallel to the plates of the stator laminations. As a result, the flux density along the core cross section in not uniform causing locally saturated parts in the stator module, and large amount of eddy current are introduced. This issue is extremely hard to avoid using traditional manufacturing or cutting techniques. On the counterpart, AM technology can be used tackle this issue by shape profiling of the core along the axial direction. This is can be made by building the core layers to be parallel to the flux path. Consequently, the eddy currents can be effectively limited. Also, the core losses can be significantly minimized resulting in an energy efficient electrical machine.

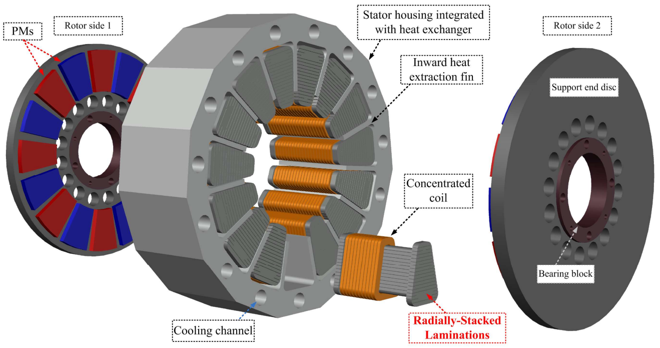

Fig. 1. Configuration of the proposed YASA axial flux machine.

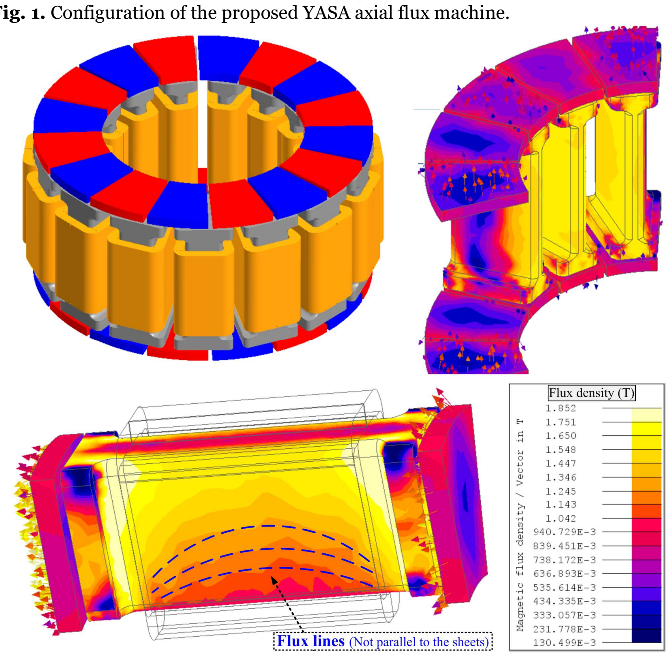

Fig. 2. Finite element 3D modeling of the baseline YASA axial flux machine.

1.3. Additive Manufacturing for Magnetic Materials

Standard laminated sheet cores can limit losses. However, it is not the best solution, because it has limited three dimensional freedom. For instance, it is hard to integrate complex cooling concepts or extend embedded functionality during the early design stage. Therefore, different studies have been reported on freeform design of ferromagnetic material enabled by AM. Lamichhane et al. [13] and Orosz et al. [14] investigated a design optimization of emerging technologies for AM electrical machines targeting minimized weight. Additionally, an advanced on/off multi-objective topology optimization is used by dividing the design space into a grid of small cells [15]. A value of zero or one can be assigned to each cell, which indicates the absence or presence of material. As a result, the material usage is significantly improved. Additionally, an enhanced heat transfer method in electrical machines is proposed using AM parts [16].

Material selection is also an important factor which affects the potential to reduce the core losses. Many research studies are made for enhancing the magnetic properties of printed material. Stornelli et al. compared the magnetic properties of additively manufacturing FeSi with different silicon content. The steel containing a 6.7wt% of Si showed inferior eddy current loss compared to Fe3wt%Si [17]. In [18], Goll et al. conducted an extensive research study showing the possibility of enhancing the magnetic properties of electrical steel components using Laser Powder Bed Fusion (LPBF) by employing electrical steel powder with a Si content of 6.7wt%, topologically optimized designs and/or multi-layered material combined with an electrical insulator. In [19], Fe6.7%Si layered structures were fabricated by LPBF and subsequently dipped in a ceramic slurry to realize an insulator surface layer. Furthermore, multi-material AM is early explored in [20]. In this study, the core of a complete electrical machine is successfully printed along with ceramic insulation. Encouraging results are obtained when the core is tested at 300°C. With the high maturity of single-material AM, different techniques can be used to build (in near-net shape) complex Fe-Si parts, which is absolutely not possible with conventional processing techniques of the steel industry. Yet, printing of laminated magnetic active parts is still practically limited and at the basic research level with small geometries and different shapes. With this being said, more in-depth research is needed to enhance and assess the properties of 3D printed magnetic materials.

In this paper, two 3D printing techniques were used to build ferromagnetic parts in order to compare the magnetic properties and to identify which one is better suited to enhance these properties. The first one is 3D micro-extrusion (also called direct ink writing or robocasting) of a powder loaded paste with computer-controlled movement in three dimensions. Different studies have reported successful attempts to print copper parts with high density using 3D micro extrusion [21–23], but no reports on Fe-Si are available. The second technique is Laser Powder Bed Fusion (LPBF). This method uses a high power-density laser to selectively melt and rapidly solidify a metallic powder bed which is deposited layer-by-layer to build a part with near net-shape. This technique is usually used for larger parts with high precision and near full density (up to 99.9%) [17,19,24,25]. A comparison between these two techniques was summarized in Table I. Using the two aforementioned AM techniques, two core samples were 3D printed using the Fe-Si powder grade and subsequently sliced to obtain thin ring shaped parts. This enable to perform a comparison to conventional electrical steel (M270-50A) sheets. The magnetic measurements on the steel sample were performed through a double coil setup.

Table I. Comparison Between Micro-Extrusion and LPBF Technologies.

Technique	3D micro-extrusion	LPBF
Shaping temperature	Feedstock material extruded at room temperature	The melting temperature can be higher than 1500°C
Energy consumption [26]	Low (energy saving) 2.8 kWh/kg	Very high 48.7 kWh/kg
Feedstock	Viscous highly powder-loaded paste	Powder bed
Internal cavities	No need for cleaning procedures after printing	Not possible to extract the powder
Binder	Needs organic binder	Not used
Powder quality	Relatively larger particle sizes	Smaller particle sizes for higher flowability
XY Resolution **Z Resolution**	20 – 65 µm 50 - 100 µm	20 – 200 µm 20 – 200 µm
Build rates [27]	Typically 30-100 cm³/h, up to 250 cm³/h in large printers	Typically 25-90 cm³/h, up to 1,000 cm³/h in large printers
Postprocesses	Sintering in a furnace with controlled atmosphere	Annealing in a normal furnace
Multi-material printing	Possible using multi-nozzle printers	Not possible yet for metal ceramic
Strengths	• Printing small details and thin walls • Broad range of materials	• Printing near net shape parts with high precision and large design freedom • Lower cost for larger parts

2. Material and 3D Printing Methods

2.1. Powder Morphology

To investigate the effect of different 3D printing techniques, two FeSi ring cores were manufactured by 3D micro extrusion and LPBF respectively. A FeSi powder with 3wt% of Si (Fe3Si, Sandvik Osprey) was selected for both samples due to its lower brittleness and hardness compared to Fe6.5Si.

Despite having the same chemical composition, the powders used for both samples are selected with different particle sizes. For 3D micro extrusion, the particles have relatively larger size that is suitable for the nozzle size and the additives. However, in LPBF, the particle sizes have to be smaller for higher flowability in the powder bed.

The morphology of the powder was analyzed by scanning electron microscopy (SEM, XL30 FEI) and the Particle Size Distribution (PSD) was characterized using a LS 13 320 particle size analyzer (Beckman Coulter™) as shown in Fig. 3. The powder chemical composition was in a good agreement with the supplier's datasheet, and the flow rate of the powder was acceptable. The powder has spherical particles with exception for few particles which showed an elongated shape. Fine satellites were observed on the surface of bigger particles. In powder used for 3D micro extrusion, the PSD analysis (Fig. 3(b)) resulted in d10, d50 and d90 of 5.69, 20.42 and 43.42 µm. In LPBF, the powder has spherical particles with the size of 29–58 µm, with a median diameter of 38 µm (d50) as shown in Fig 3(d).

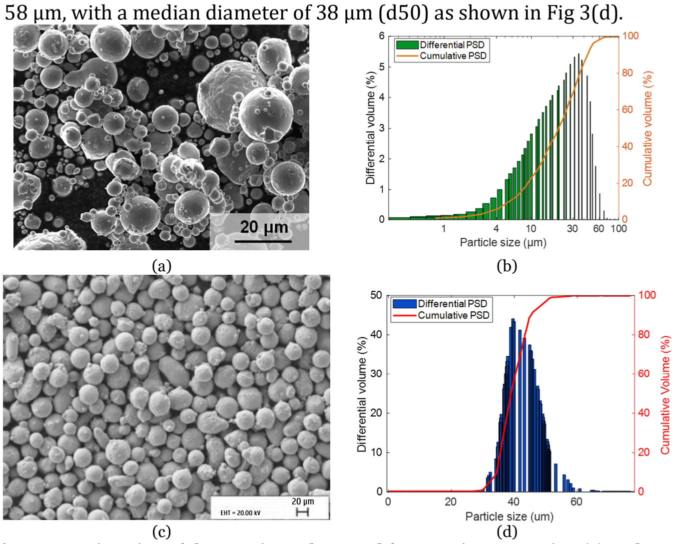

Fig. 3. SEM imaging of the Fe3Si powders used for 3D micro-extrusion (a) and LPBF (c) and their particle size distribution, respectively (b,d).

2.2. Micro Extrusion

To print the first ring core using 3D micro extrusion, the powder was combined with a propanol based binder system in a speedmixer (Hauschild Speedmixer DAC1100) to obtain a viscous highly powder-loaded paste. This latter was transferred into a syringe and extruded at room temperature through a 400µm diameter nozzle using a 3Dn-450HP n-Scrypt printing machine equipped with a needle valve extrusion system operating at constant air pressure. The green part obtained, shown in Fig. 4 (a), was then dried at room temperature prior to the post-printing treatment, i.e. thermal debinding and pressureless sintering, that was performed in a horizontal tube furnace under reducing atmosphere. Ar+5% was the gas mixture employed for the thermal debinding which was carried out by heating at 5°C/min up to 1030°C for 2 hours. Then the temperature was further increased by heating at 2°C/min up to 1400°C for 2 hours in 100% H_2 atmosphere. The complete heat treatment cycle is shown in Fig. 5.The sintered part was removed from the furnace upon complete cooling (Fig. 4(b)). The Fe3Si ring was finally sliced into thin 0.5mm laminations using wire electrical discharge machining (EDM) before it is coated by varnish, as shown in Fig. 4(c). The main reason for using EDM is to save energy during the sintering process. To anneal a high number of samples at the same time, a larger industrial furnace is needed. Additionally, printing individual laminations in a cascaded process requires much time especially if the printer has a limited print area. For the magnetic characterization, the primary and secondary coils were wounded toroidally around the ring core to prepare it for measurements as shown in Fig. 4(d).

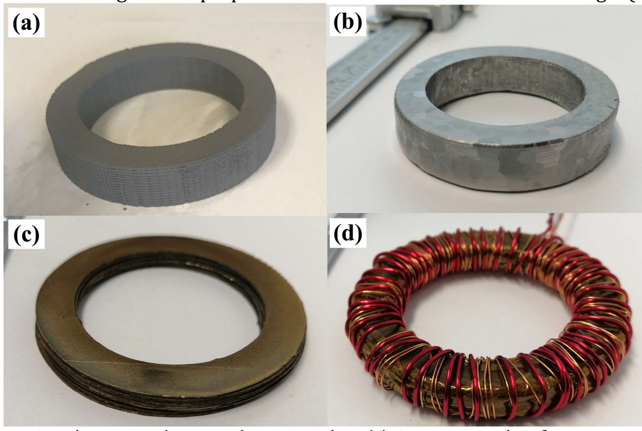

Fig. 4. AM ring core using 3D micro-extrusion. (a) Green part printed at room temperature. (b) After sintering. (c) Slicing into 0.5mm laminations. (d) Final test sample.

2.3. LPBF

The second ring core was also printed from the Fe3Si powder using LPBF. The printing parameters are listed in Appendix A. The printer and the sample are shown Fig. 6 (a, b). The heat treatment process is performed in a graphite chamber Webb-107 vacuum furnace. The annealing cycle is also shown in Fig. 5. The sample is heated in a 0.1 mBar vacuum environment up to a temperature of 1200°C, held for one hour, followed by slow furnace cooling. The printed near net shape part is then sliced into thinner 0.5mm-laminations by wire EDM cutting before it was heat treated and varnish coated as shown in Fig. 6 (c). Finally, the ring core is prepared with two coils as shown in Fig. 6 (d, e). The magnetic properties of both the ring cores were measured and compared to a M270-50A conventional electrical steel ring core sample with a lamination thickness of 0.5mm, cf. Fig. 7.

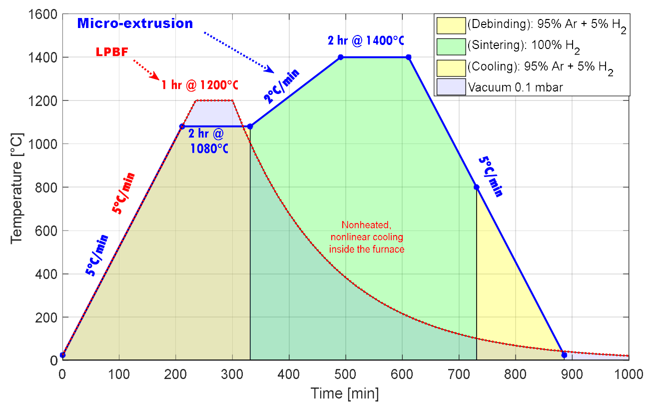

Fig. 5. Heat treatment cycle for both of 3D micro-extrusion and LPBF.

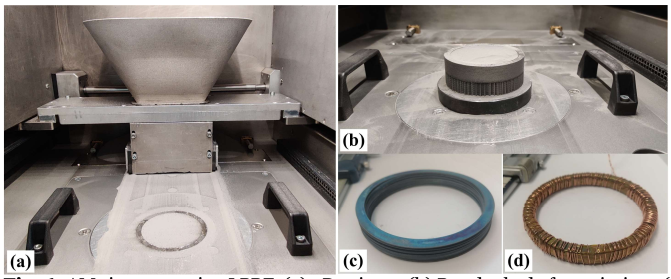

Fig. 6. AM ring core using LPBF. (a) 3D printer. (b) Powder bed after printing. (c) Slicing into 0.5mm laminations. (d) Placing test coils. (e) Final test sample.

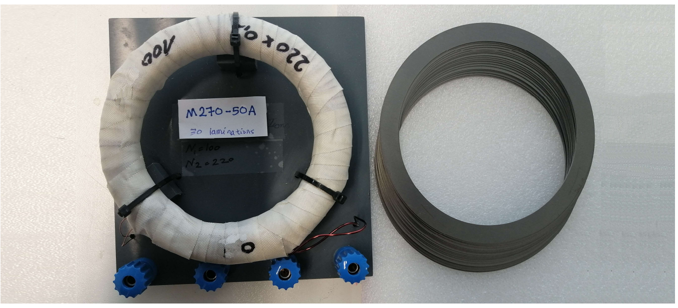

Fig. 7. A ring core of conventional non-oriented electrical steel (M270-50A).

3. Measurement Approach for the Magnetic Material

3.1. Test Setup

Different approaches can be used to perform magnetic material measurements based on the sample shape and dimensions: the Epstein frame [28], the single sheet tester [29] or the ring core [30]. The main function of all these devices is to create a closed magnetic path for both primary and secondary coils. In the present study, the ring shape was selected in order to avoid the airgap that is present in the other approaches. Therefore, no calibration was needed. The magnetic properties of the three test samples are listed and explained as follows.

- M270-50A non-oriented conventional steel laminations (D_o = 80mm, D_i = 70mm, thickness= 0.5mm).
- 3D printed ring core using micro-extrusion (D_o = 60mm, D_i = 40mm, thickness= 0.5mm).
- 3D printed LPBF core (D_o = 80mm, D_i = 70mm, thickness= 0.5mm).

As noticed, the 3D printed samples have different dimensions. For a fair comparison between the thermal behavior, different number of lamination to ensure a good weight balance. In terms of the loss comparison, the measured iron losses are reported using the specific value in W/kg.

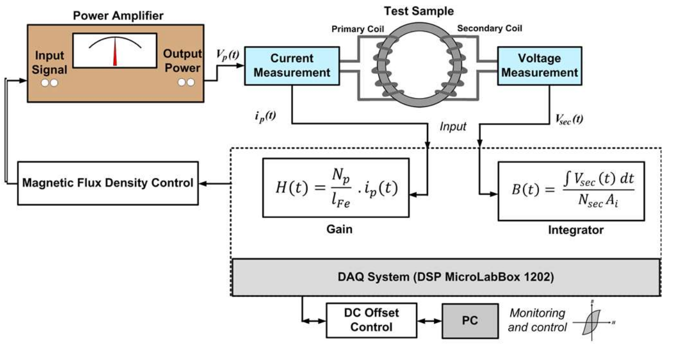

Fig. 8. Schematic for Magnetic measurement of a ring core.

Fig 8 shows magnetic measurements schematic for a ring core. Fig. 9 shows the corresponding test setup for magnetic material characterization. The setup and components are as follows:

- Power amplifier (Spitzenberger) with variable AC voltage and frequency.
- dSpace MicroLabBox 1202 for data acquisition and real time interface for the time-varying magnetic induction $B_c(t)$ and field strength $H_c(t)$.
- Voltage and current sensors for the measurements of the primary current and the secondary voltage; $I_p(t)$ and $V_{sec}(t)$.
- PC installed with dSpace control disc software to monitor all waveforms and the hysteresis loops.
- Thermal camera for temperature monitoring.
- High rating power resistor to be connected in series with the primary coil to limit high currents at very low frequencies.

To measuring the magnetic properties, the field strength $H(t)$ and the magnetic flux density $B(t)$ should be measured simultaneously. The field strength can calculated from the current in primary coil $i_p(t)$ as follows:

$$H(t) = \frac{N_p}{l_{Fe}} . i_p(t) \tag{1}$$

Where, N_p is the number of turns in the primary coil and l_{Fe} is the magnetic path length. The corresponding magnetic flux density as a function in time can be estimated by the integration of the back EMF induced into the secondary winding which have a turns number of N_{sec}.

$$B(t) = \frac{1}{N_{sec} A_{Fe}} \int V_{sec}(t)\, dt \tag{2}$$

where, A_{Fe} is the cross section area of the ring core. Additionally, The average value of the specific core loss in Watt/kg is obtained from the measured dynamic $B(H)$ loop, during one period of the fundamental frequency f as follows:

$$P_{core} = \frac{f}{\rho} \int_0^{1/f} H(t)\ dB(t) \tag{3}$$

$$P_{core} = \frac{N_p\, f}{N_{sec}\, A_{Fe}\, l_{Fe}\, \rho} \int_0^{1/f} i_p(t)\, V_{sec}(t)\ dt \tag{4}$$

where ρ is the mass density of the ring core in kg/m3.

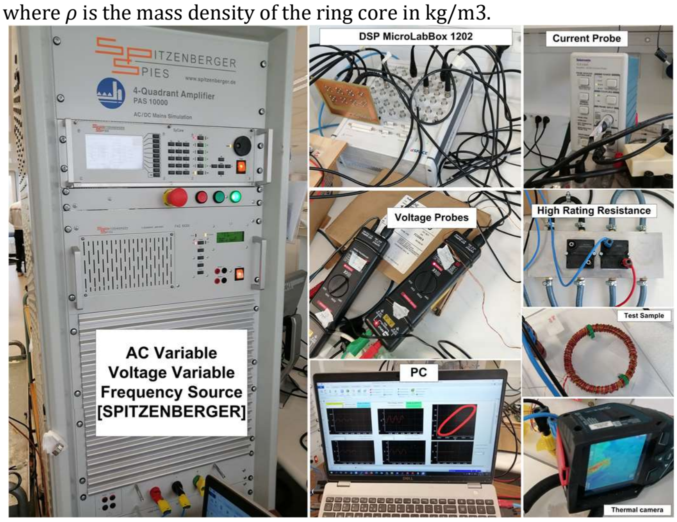

Fig. 9. Test platform for magnetic material measurements.

3.2. DC Offset Control

In order to monitor the time-varying magnetic induction $B_c(t)$ and field strength $H_c(t)$, some calculations are made based on the sample type using equations (1-4). The waveform of the instantaneous field strength is shown in Fig. 10 for one of the samples at a fixed frequency level of 200 Hz. The corresponding secondary voltage is also measured as shown in Fig. 11. It is noticed that there is a small DC offset in the sinusoidal voltage waveform. The main issue of this undesired offset is that it will case an increasing ramp function in the flux density waveform which rises continuously with time after the integration of the secondary voltage. That is why this small DC offset must be eliminated. Fig. 12 shows the magnetic flux density waveform before and after offset control. It is clear that the ramp function is removed after offset control and the flux density is not increasing to illogical values. This comparison is also made for the BH loop as shown in Fig. 13. Obviously, after DC offset control, all the BH loops are almost identical under the same field intensity. Therefore, the measurements accuracy is very high and the results are reliable.

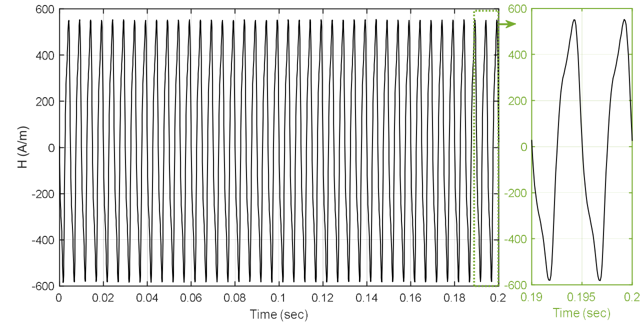

Fig. 10. The instantaneous magnetic field strength at 200Hz.

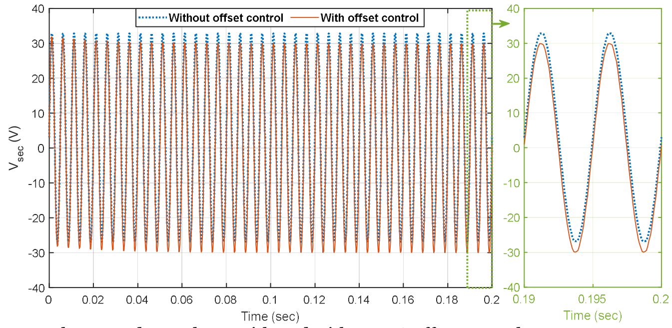

Fig. 11. The secondary voltage with and without DC offset control at 200Hz.

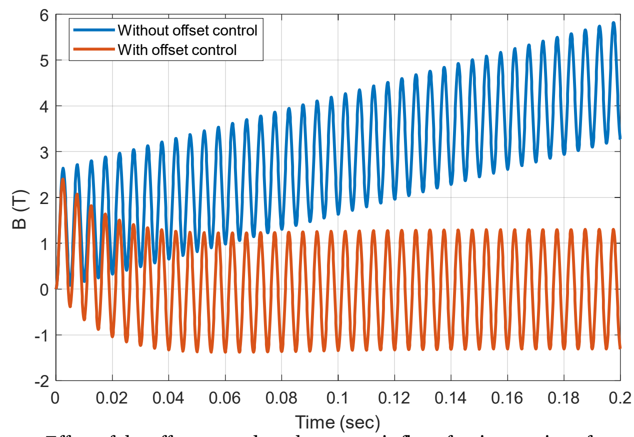

Fig. 12. Effect of the offset control on the magnetic flux after integration of secondary voltage waveform at 200Hz.

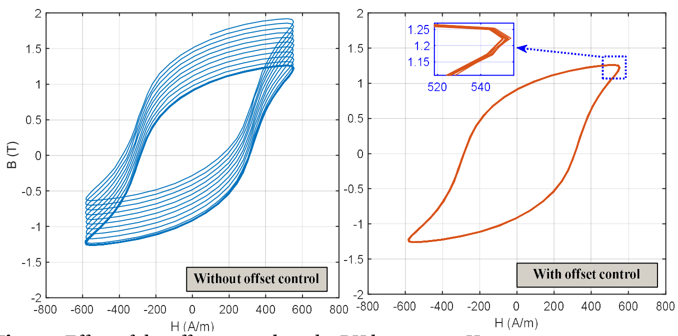

Fig. 13. Effect of the offset control on the BH loop at 200Hz.

4. Results and discussion

4.1. Core losses

The results are first compared at 50 Hz. In Fig. 14, 15, the BH loops are compared at 1T and 1.5T, respectively. The area of the BH loop is the highest for the LPBF, and the lowest for the conventional steel. The micro-extruded 3D printed ring has an intermediate BH loop. The variation of the specific core losses with the magnetic induction at 50Hz is shown in Fig. 16. It is clear that the micro-extruded part has relatively lower core losses compared to the LPBF equivalent. This difference is also noticed in Fig. 17 from the thermal profile under the same ampere-turns excitation. For a fair comparison between the thermal behavior, different number of lamination to ensure a good weight balance since the samples have different dimensions.

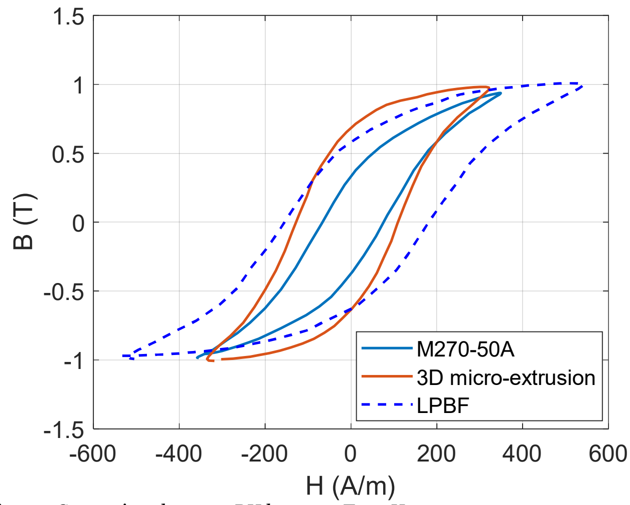

Fig. 14. Comparison between BH loops at 1T, 50 Hz.

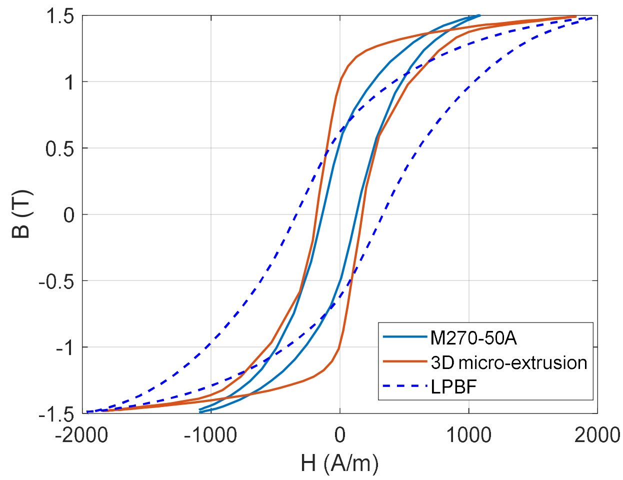

Fig. 15. Comparison between BH loops near saturation level at 1.5T, 50 Hz.

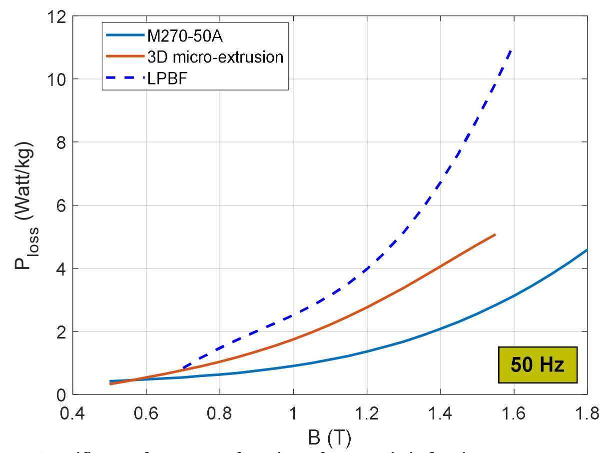

Fig. 16. Specific core losses as a function of magnetic induction at 50Hz.

In order to measure the hysteresis loss component separately without eddy current effect, quasi-static excitation measurements are conducted at a very lower frequencies of 1 Hz, as shown in Fig. 18. Interestingly, unlike the LPBF part, the micro-extruded ring has only a slight increase in the losses with respect to standard electrical steel. Therefore, it can be concluded that 3D micro-extrusion of Fe-Si at room temperature followed by controlled debinding and furnace sintering is more favorable for the magnetic properties than LPBF followed by thermal annealing.

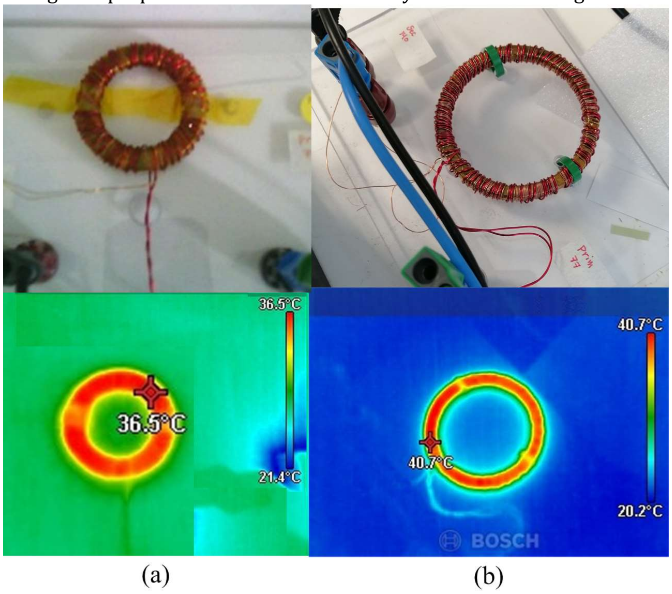

Fig. 17. Thermal profile for the 3D printed samples at 50 Hz under the same ampere turn excitation. (a) 3D micro-extrusion, (b) LPBF.

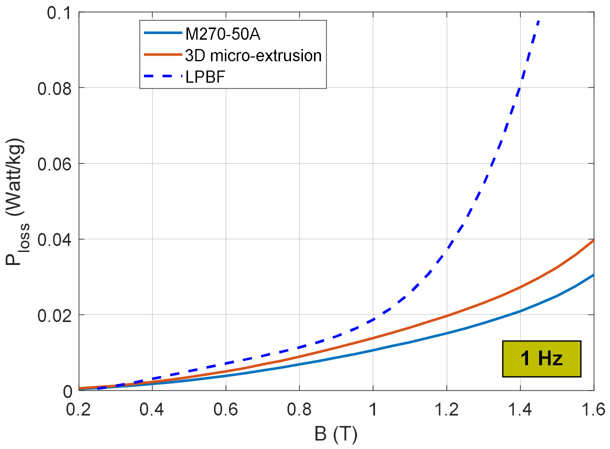

Fig. 18. Quasi-static measurements for the specific hysteresis losses as a function of magnetic induction at 1Hz.

4.2. *Microstructure Characterization*

In order to further understand the differences between the magnetic materials, the microstructural characterization was performed after cutting the thin rings and polishing the x-y surface up to 1μm prior to external etching (Struers LectroPol-5) up to 60 seconds using an electrolyte consisting in 90vol% of CH3COOH and 10vol% of HCl4 . Electron backscatter diffraction (EBSD) was performed in a scanning electron microscope (SEM, Quanta 450 FEI) for the three polished rings to compare the texture and the microstructure.

Fig. 19 shows a microstructural comparison, through EBSD imaging, of the x-y plane for the three ring cores together with the Inverse Pole Figures (IPF) along the building direction (BD). The M270-50A material exhibited equiaxed grains with a prevalence of the <111> crystallographic direction aligned to ND. This texture does not represent the ideal case for laminated steel since it excludes the easy <001> magnetization direction to be oriented parallel to the plane of the sheet as required for high quality NOES [31]. On the other hand, the LPBF ring core resulted in a relatively pronounced texture with the <001> lattice direction along BD (as shown in Fig. 19e), which is favorable for magnetic properties. For this material a finer grain size was observed in the cross-section perpendicular to the BD after annealing. Due to the process features, the grains are expected to have a columnar morphology along the building direction [18]. Furthermore, in the LPBF printed sample the presence of pores (with a size up to 250μm), as indicated by the yellow arrows in Fig. 19(b), was observed and attributed to the printing process. A different result was observed for the 3D micro-extrusion ring which demonstrated the presence of large grains (up to 1mm in size) of randomly scattered crystal orientations without pronounced alignment of the <100> crystallographic direction parallel to BD. It needs to be notified, though, that the number of grains characterized for texture measurement was generally not sufficient for a complete statistical representation. Nevertheless, the lack of a strong texture, observed for a low number of grains, strongly suggests the presence of a random texture for the micro-extruded sample. Moreover, a large grain size is generally considered a favorable microstructural feature leading to reduced hysteresis losses at low frequencies. The microstructural analysis highlighted the presence of isolated closed porosities located inside the grains and at the grain boundaries. Few bigger pores (with a maximum size of 138μm) were identified at the grain boundaries as pointed by the green arrows in Fig. 19(c).

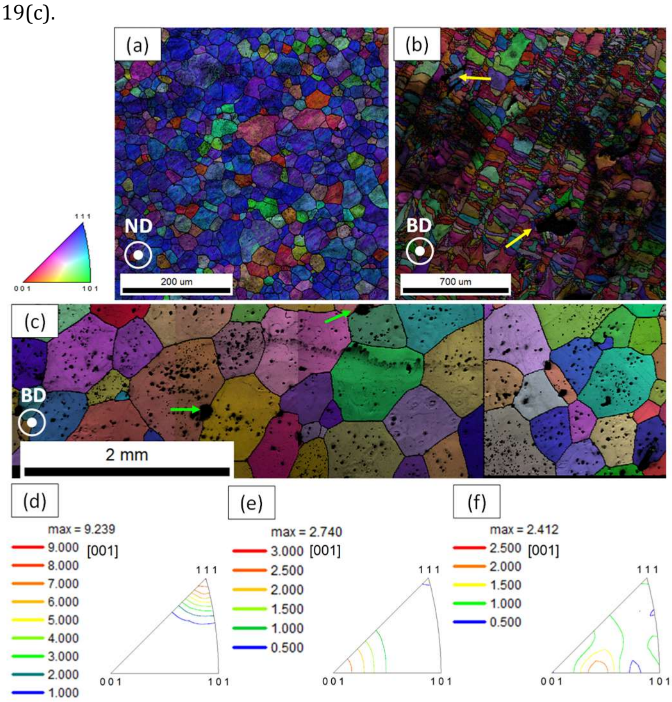

Fig. 19. Microstructure analysis shown through EBSD maps (a) M270-50A, (b) LPBF, (c) 3D micro-extrusion. The texture analysis along the z axis, i.e. the normal direction (ND) or building direction (BD) is shown (d, e, f) for M270-50A, LPBF and 3D micro-extrusion, respectively.

Microstructural features such crystallographic texture and crystal defects such as grain boundaries, dislocation density and precipitates can affect the magnetic core loss. Additionally, losses may be affected by the presence of free surfaces. The latter unavoidably introduce closure domains in ferromagnetic materials so as to minimize the magnetostatic energy. The residual pores represent free surfaces in the material and thus will lead to an increased density of domain walls, which in turn may give rise to an increase of (discontinuous) domain wall jumps producing an increased hysteresis loss during magnetization. For both the LPBF and 3D micro-extrusion processes, the presence of pores was observed, so for the 3D printed materials the domain wall density is higher compared to the conventional material and this could explain the higher losses. It must be notified that although the LPBF ring core exhibited the best texture, it showed inferior magnetic core loss compared not only to the conventionally manufactured steel but also compared to the micro-extruded material, which is probably on the account of increased pore densities. It requires a complete quantitative characterization of the entire scope of microstructural features to establish a comprehensive correlation between magnetic properties and microstructure.

5. Potentials of 3D Micro-Extrusion

3D micro-extrusion offers the possibility to print parts in near-net shape, which is not possible with conventional processing techniques. An example is shown in Fig. 20 for a clock spring design which can be used to limit eddy currents at high frequency. Additionally, using this technology, it is possible control the silicon (Si) content in the steel powder. The Si content reduces the electrical resistivity (with a max at 6.5%) of the steel and therefore reduces the eddy current loss. This is even more important with widening scope of applications to higher frequency.

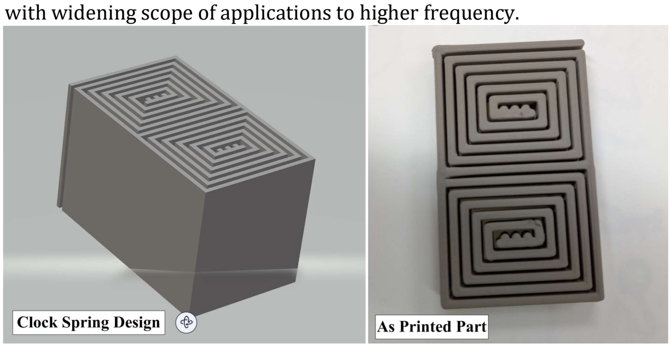

Fig. 20. 3D micro-extrusion of parts in near-net shape.

Moreover, 3D micro-extrusion technologies allow multi-material 3D Printing of different layers of magnetic and non-magnetic materials. Accordingly, complete AM parts can be built into a near-net-shape without the need for a mechanical post-process to slice into laminations. An example is shown in Fig. 21 (a), which is a ring core with a serpentine cross-section area. An insulating layer is deposited between the layers of the magnetic material. This shape is selected specifically to avoid any cracking during the thermal treatment due to the difference in thermal expansion coefficients of the materials.

Using a multi-nozzle 3D printer, the shape is built using micro-extrusion, as shown in Fig 21(b). A high-quality Fe-Si powder is used enabling the deposition of thin layers with a mean thickness of 200μm. A ceramic insulator is used as an interlayer with a mean thickness of 50 μm. It is noticed that a good adhesion is achieved between the Fe-Si and insulator layers. Additionally, the non-linear interface between those layers will result in extra mechanical interlocking. A Zirconium dioxide (ZrO_2) is used for the insulation layer, also known as zirconia. It is one of the common ceramic materials that adopts a monoclinic crystal structure at room temperature and transitions to tetragonal and cubic at higher temperatures. Zirconia has great hardness and excellent mechanical properties at high temperatures. The material datasheet is provided in [32].

(a)

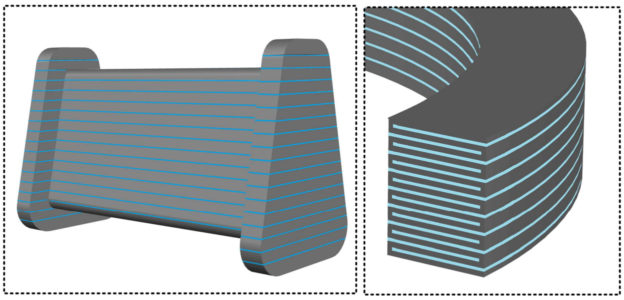

(b)

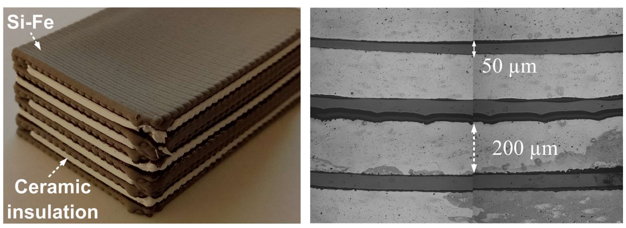

Fig. 21. Multi-material 3D printing. (a) Serpentine shape. (b) Cross section view of printed part. (c) EBSD analysis.

The multi-material layered part is expected to achieve improved magnetic properties with much lower eddy current losses compared to the printed samples discussed above, since it is printed in near-net-shape without any destructive post-processing such as (laser cutting, interlocking, welding, stacking, etc.).

6. Conclusions

This paper introduces magnetic properties evaluation for 3D printed magnetic material. Using different AM techniques, different samples are printed utilizing the same chemical composition powder. Two different AM techniques are used to print the Fe-Si ring core parts, which are 3D micro-extrusion and LPBF. The pros and cons of both techniques are highlighted and compared. Additionally, the core losses are measured and compared with conventional steel laminations. Also, the effect of the DC offset on the BH waveforms is explained. It is proved that controlling the DC offset results in a reliable measurements of the magnetic properties. It is obvious that the properties of 3D printed materials are getting closer and closer to those of standard electrical steel. Moreover, by measuring the specific core losses at very low frequency, it can be concluded that 3D micro-extrusion of Fe-Si at room temperature followed by a sintering process allows to obtain better magnetic properties than thermally treated LPBF material. The microstructural investigation highlighted a substantial difference in the final materials manufactured using the two different AM processes both in terms of grain size and texture. Finally, the future trend of 3D multi-material printing is discussed, showing the huge potential of this technology for the manufacturing of innovative magnetic material parts.

Appendix A

The printing parameters of the LPBF are summarized in Table II. The printing was performed in a nitrogen environment, with oxygen purged from the chamber below 0.1% content. The contour scanning has 350 W laser power at 0.75 m/s.

Table II. LPBF printing parameters.

Optimized Parameter	Unit	Value
Laser power	W	350
Scanning velocity	mm/s	750
Volumetric energy density	J/mm3	77
Fixed Parameter	**Unit**	**Value**
Layer thickness	μm	50
Hatch distance	μm	120
Laser spot size	μm	~120
Scan strategy	-	Stripes
Print environment	-	Nitrogen
Preheating	-	No
Remelting	-	No
Print chamber oxygen content	%	~0.1

Declaration of Competing Interests

The authors declare that they have no known competing interests that influences the work reported in this paper.

Acknowledgements

This research is financially supported by the Research Foundation—Flanders (FWO) in the project (S001721N) entitled Multi-Material Additive Manufacturing for Electrical Machines with increased performance (AM4EM).

References

[1] S. Lammers, G. Adam, H.J. Schmid, R. Mrozek, R. Oberacker, M.J. Hoffmann, F. Quattrone, B. Ponick, Additive Manufacturing of a lightweight rotor for a permanent magnet synchronous machine, in: 2016 6th Int. Electr. Drives Prod. Conf., IEEE, 2016: pp. 41–45. https://doi.org/10.1109/EDPC.2016.7851312.

[2] A. Selema, M.N. Ibrahim, P. Sergeant, Metal Additive Manufacturing for Electrical Machines: Technology Review and Latest Advancements, Energies. 15 (2022) 1076. https://doi.org/10.3390/en15031076.

[3] A. Selema, M.N. Ibrahim, P. Sergeant, Additively Manufactured Ultralight Shaped-Profile Windings for HF Electrical Machines and Weight-Sensitive Applications, IEEE Trans. Transp. Electrif. 8 (2022) 4313–4324. https://doi.org/10.1109/TTE.2022.3173126.

[4] H.-S. Hong, H.-C. Liu, G.-C. Jeong, J. Lee, Design of high-end SynRM based on 3D printing technology, in: 2016 IEEE Conf. Electromagn. F. Comput., IEEE, 2016: pp. 1–1. https://doi.org/10.1109/CEFC.2016.7816043.

[5] R. Ranjan, J. Tangudu, Thermal design of high power-density additively-manufactured induction motors, in: 2014 IEEE Energy Convers. Congr. Expo., IEEE, 2014: pp. 1325–1331. https://doi.org/10.1109/ECCE.2014.6953554.

[6] J. Waterman, A. Clucas, T.B. Costa, Y. Zhang, J. Zhang, Numerical modeling of 3D printed electric machines, in: 2015 IEEE Int. Electr. Mach. Drives Conf., IEEE, 2015: pp. 1286–1291. https://doi.org/10.1109/IEMDC.2015.7409227.

[7] A. Mahmoudi, Hew Wooi Ping, N.A. Rahim, A comparison between the TORUS and AFIR axial-flux permanent-magnet machine using finite element analysis, in: 2011 IEEE Int. Electr. Mach. Drives Conf., IEEE, 2011: pp. 242–247. https://doi.org/10.1109/IEMDC.2011.5994853.

[8] A. Mohamed, A. Hemeida, A. Rasekh, H. Vansompel, A. Arkkio, P. Sergeant, A 3D Dynamic Lumped Parameter Thermal Network of Air-Cooled YASA Axial Flux Permanent Magnet Synchronous Machine, Energies. 11 (2018) 774. https://doi.org/10.3390/en11040774.

[9] A. Selema, Development of a Three-Phase Dual-Rotor Magnetless Flux Switching Generator for Low Power Wind Turbines, IEEE Trans. Energy Convers. 35 (2020) 828–836. https://doi.org/10.1109/TEC.2019.2955009.

[10] H. Vansompel, P. Leijnen, P. Sergeant, Multiphysics Analysis of a Stator Construction Method in Yokeless and Segmented Armature Axial Flux PM Machines, IEEE Trans. Energy Convers. 34 (2019) 139–146. https://doi.org/10.1109/TEC.2018.2862622.

[11] H. Vansompel, P. Sergeant, L. Dupre, A. Van den Bossche, Evaluation of a Simple Lamination Stacking Method for the Teeth of an Axial Flux Permanent-Magnet Synchronous Machine With Concentrated Stator Windings, IEEE Trans. Magn. 48 (2012) 999–1002. https://doi.org/10.1109/TMAG.2011.2173161.

[12] N. Taran, G. Heins, V. Rallabandi, D. Patterson, D.M. Ionel, Evaluating the Effects of Electric and Magnetic Loading on the Performance of Single and Double Rotor Axial Flux PM Machines, IEEE Trans. Ind. Appl. (2020) 1–1. https://doi.org/10.1109/TIA.2020.2983632.

[13] T.N. Lamichhane, L. Sethuraman, A. Dalagan, H. Wang, J. Keller, M.P. Paranthaman, Additive manufacturing of soft magnets for electrical machines—a review, Mater. Today Phys. 15 (2020) 100255. https://doi.org/10.1016/j.mtphys.2020.100255.

[14] T. Orosz, A. Rassõlkin, A. Kallaste, P. Arsénio, D. Pánek, J. Kaska, P. Karban, Robust Design Optimization and Emerging Technologies for Electrical Machines: Challenges and Open Problems, Appl. Sci. 10 (2020) 6653. https://doi.org/10.3390/app10196653.

[15] Y. Hidaka, T. Sato, H. Igarashi, Topology Optimization Method Based on On–Off Method and Level Set Approach, IEEE Trans. Magn. 50 (2014) 617–620. https://doi.org/10.1109/TMAG.2013.2285379.

[16] R. Wrobel, A. Hussein, Design Considerations of Heat Guides Fabricated Using Additive Manufacturing for Enhanced Heat Transfer in Electrical Machines, in: 2018 IEEE Energy Convers. Congr. Expo., IEEE, 2018: pp. 6506–6513. https://doi.org/10.1109/ECCE.2018.8557559.

[17] and R.M. Stornelli, Giulia, Antonio Faba, Andrea Di Schino, Paolo Folgarait, Maria Rita Ridolfi, Ermanno Cardelli, Properties of Additively Manufactured Electric Steel Powder Cores with Increased Si Content, Materials (Basel). 14 (2021). https://doi.org/10.3390/ma14061489.

[18] D. Goll, J. Schurr, F. Trauter, J. Schanz, T. Bernthaler, H. Riegel, G. Schneider, Additive manufacturing of soft and hard magnetic materials, Procedia CIRP. 94 (2020) 248–253. https://doi.org/10.1016/j.procir.2020.09.047.

[19] J.W.J. Bonuk Koo, Min-Sun Jang, Yeong Gyun Nam, Sangsun Yang, Jihun Yu, Yong Ho Park, Structurally-layered soft magnetic Fe-Si components with surface insulation prepared by shell-shaping selective laser melting, Appl. Surf. Sci. 553 (2021). https://doi.org/10.1016/j.apsusc.2021.149510.

[20] TUChemnitz, 3D multi-material printing, (2020). https://www.tu-chemnitz.de/etit/ema/AMMM/index.php (accessed June 17, 2022).

[21] G. Singh, J.-M. Missiaen, D. Bouvard, J.-M. Chaix, Copper extrusion 3D printing using metal injection moulding feedstock: Analysis of process parameters for green density and surface roughness optimization, Addit. Manuf. 38 (2021) 101778. https://doi.org/10.1016/j.addma.2020.101778.

[22] S. Khalilpourazary, The effect of the ECAP process on the copper micro gears produced by the forward micro-extrusion process, CIRP J. Manuf. Sci. Technol. 35 (2021) 53–62. https://doi.org/10.1016/j.cirpj.2021.05.010.

[23] X. Ma, X. Li, G. Petrossian, A. Ortiz, M. Komarasamy, S. Whalen, G. Grant, S. Mathaudhu, N. Overman, Porosity evolution during heating of copper made from powder by friction extrusion, Materialia. 21 (2022) 101341. https://doi.org/10.1016/j.mtla.2022.101341.

[24] L. Kaden, G. Matthäus, T. Ullsperger, H. Engelhardt, M. Rettenmayr, A. Tünnermann, S. Nolte, Selective laser melting of copper using ultrashort laser pulses, Appl. Phys. A. 123 (2017) 596. https://doi.org/10.1007/s00339-017-1189-6.

[25] S.D. Jadhav, S. Dadbakhsh, L. Goossens, J.-P. Kruth, J. Van Humbeeck, K. Vanmeensel, Influence of selective laser melting process parameters on texture evolution in pure copper, J. Mater. Process. Technol. 270 (2019) 47–58. https://doi.org/10.1016/j.jmatprotec.2019.02.022.

[26] D.A.G. to M.A. Manufacturing, Energy Consumption in Metal Additive Manufacturing, (2019). https://www.digitalalloys.com/blog/energy-consumption-metal-additive-manufacturing/ (accessed December 21, 2022).

[27] All3dp; Digital Maker Magazine, Selective Laser Melting Guide, (2021). https://all3dp.com/1/selective-laser-melting-guide/ (accessed December 21, 2022).

[28] P. Marketos, S. Zurek, A.J. Moses, A Method for Defining the Mean Path Length of the Epstein Frame, IEEE Trans. Magn. 43 (2007) 2755–2757. https://doi.org/10.1109/TMAG.2007.894124.

[29] Y. Zhang, J. Zhao, L. Wang, Y. Guo, Z. Li, J. Huang, Optimization of Two-Dimensional Rotational Single Sheet Tester, in: 2019 22nd Int. Conf. Electr. Mach. Syst., IEEE, 2019: pp. 1–4. https://doi.org/10.1109/ICEMS.2019.8922126.

[30] A. Kahveci, P. Szary, F. Herget, A.K. Putri, K. Hameyer, Methods for hysteresis losses determinations at non-standard ring core geometries equivalent to Epstein measurements, in: 2016 6th Int. Electr. Drives Prod. Conf., IEEE, 2016: pp. 135–142. https://doi.org/10.1109/EDPC.2016.7851325.

[31] L. Kestens, S. Jacobs, Texture Control During the Manufacturing of Nonoriented Electrical Steels, Texture, Stress. Microstruct. 2008 (2008) 1–9. https://doi.org/10.1155/2008/173083.

[32] Additiveplus, 3DCeram Zirconia 3Y 3D Printing Paste, (2021). https://additiveplus.com/docs/nuancier_3DMIX_2021.pdf (accessed December 21, 2022).